RESEARCH ARTICLE
PLANETARY SCIENCES

Earth and Planetary Physics
8: 326–337, 2024
doi: 10.26464/epp2024013

Statistical study of magnetic holes in the upstream region of Mercury's bow shock

GuoQiang Wang[1,2,3], SuDong Xiao[1,2], MingYu Wu[1,2], YuanQiang Chen[1,2], and TieLong Zhang[1,2,4,5*]

[1]Institute of Space Science and Applied Technology, Harbin Institute of Technology, Shenzhen 518055, China;

[2]Shenzhen Key Laboratory of Numerical Prediction for Space Storm, Harbin Institute of Technology, Shenzhen 518055, China;

[3]Mengcheng National Geophysical Observatory, University of Science and Technology of China, Hefei 230026, China;

[4]Chinese Academy of Sciences Center for Excellence in Comparative Planetology, Hefei 230026, China;

[5]Space Research Institute, Austrian Academy of Sciences, Graz, Austria

Key Points:

- The magnetic holes with a duration of 0.1–100 s in the upstream region of Mercury's bow shock can be divided into two groups according to their durations' distribution.
- Both groups of the magnetic holes are more likely to occur during the weak interplanetary magnetic field.
- The foreshock can increase (decrease) the occurrence rate of the magnetic holes in the group with small (large) durations.

Citation: Wang, G. Q., Xiao, S. D., Wu, M. Y., Chen, Y. Q., and Zhang, T. L. (2024). Statistical study of magnetic holes in the upstream region of Mercury's bow shock. *Earth Planet. Phys.*, *8*(2), 326–337. http://doi.org/10.26464/epp2024013

Abstract: Magnetic holes are magnetic depression structures that exist widely in many plasma environments. The magnetic holes with durations of >1 s in the solar wind at Mercury's orbit have drawn much attention, but the properties of the magnetic holes with shorter durations are still unclear. Here, we investigate the magnetic holes with durations of 0.1–100 s in the upstream region of Mercury's bow shock based on observations by the MESSENGER (MErcury Surface, Space ENvironment, GEochemistry, and Ranging) spacecraft. They can be divided into two groups according to the distribution of their duration: small-duration magnetic holes (SDMHs, <0.6 s) and large-duration magnetic holes (LDMHs, >0.6 s). The duration of each group approximately obeys a log-normal distribution with a median of ~0.25 s and 3 s, respectively. Approximately 1.7% (32.6%) of the SDMHs (LDMHs) reduce the magnetic field strength by more than 50%. For both groups, some structures have a linear or quasi-linear polarization, whereas others have an elliptical polarization. The magnetic hole events in both groups tend to have a higher rate of occurrence when the interplanetary magnetic field strength is weaker. Their occurrence rates are also affected by Mercury's foreshock, which can increase (decrease) the occurrence rate of the SDMHs (LDMHs). This finding suggests that Mercury's foreshock might be one source of the SDMHs and that the foreshock can destroy some LDMHs. These observations suggest that a new group of magnetic holes with durations of <0.6 s exist in the upstream region of Mercury's bow shock.

Keywords: magnetic hole; solar wind; Mercury; foreshock

1. Introduction

Magnetic holes with a size of several to tens of ion gyroradii, first reported by Turner et al. (1977), are a kind of magnetic depression structures (Stevens and Kasper, 2007). They exist widely in many astrophysical plasma environments, such as the solar wind (Stevens and Kasper, 2007; Madanian et al., 2020; Potapov, 2020; Volwerk et al., 2021), planetary magnetosheaths (Soucek et al., 2008; Balikhin et al., 2009; Génot et al., 2009; Volwerk et al., 2016; Karlsson et al., 2021; Duanmu XY et al., 2023), and magnetospheres (Wang GQ et al., 2016, 2020a). Magnetic holes can be generated by ion mirror instabilities (Hasegawa, 1969; Tsurutani et al., 2011). In the solar wind, their occurrence rate decreases with an increase in the heliocentric distance from ~0.3 to 8.9 astronomical units (AU), suggesting that they might originate from somewhere within 0.3 AU (Russell et al., 2008).

In the last decade, magnetic holes with a size of ~1 ρ_i (ion gyroradius) or less have been found to be a common phenomenon existing in the terrestrial current sheet (Ge YS et al., 2011; Gershman et al., 2016; Goodrich et al., 2016; Yao ST et al., 2016, 2021; Shustov et al., 2020), planetary magnetosheaths (Huang SY et al., 2017; Liu H et al., 2019; Yao ST et al., 2019a; Goodrich et al., 2021; Wu MY et al., 2021; Chen YJ et al., 2022), and the upstream region of the terrestrial and Martian bow shocks (Yao ST et al., 2019b; Wang GQ et al., 2020b, d, 2021b). These sub-ion-scale structures can trap electrons with an energy up to a few 10^5 eV (Balikhin et al., 2012; Sun WJ et al., 2012). In addition, electron cyclotron waves, whistler mode waves (or lion roars), and electrostatic solitary waves are able to be generated inside them in the magnetosheath (Maksi-

First author: G. Q. wang, wanggq@hit.edu.cn
Correspondence to: T. L. Zhang, Tielong.Zhang@oeaw.ac.at
Received 30 NOV 2023; Accepted 13 JAN 2024.
First Published online 01 MAR 2024.

movic et al., 2001; Huang SY et al., 2018, 2019; Sun JC et al., 2019; Yao ST et al., 2019a). Thus, they might play an important role in transporting electrons (Balikhin et al., 2012) or dissipating energy (Huang SY et al., 2017). Several generation mechanisms can explain the formation of sub-ion-scale magnetic holes, such as electron mirror instabilities (Sundberg et al., 2015; Yao ST et al., 2019b), tearing mode instabilities (Balikhin et al., 2012), the electron magnetohydrodynamics soliton model (Ji XF et al., 2014; Li ZY et al., 2016), electron vortex magnetic holes (Haynes et al., 2015), and ballooning/interchange instabilities (Shustov et al., 2019).

On the basis of observations by the MAVEN (Mars Atmosphere and Volatile EvolutioN) spacecraft, Wang GQ et al. (2021a) statistically studied the magnetic holes with durations of 0.1–100 s in the upstream region of the Martian bow shock. According to the distribution of their durations, the authors found that these magnetic holes could be divided into two groups with a duration of 0.1–2 s and 2–100 s, respectively. For each group, the durations of the magnetic holes approximately obeyed the log-normal distribution. And the magnetic holes with durations of 0.1–2 s were suggested to be sub-ion scale (Wang GQ et al., 2021a). An abundance of electron and ion dynamics can be created during the interaction between the solar wind and bow shock (Eastman et al., 1981; Hao YF et al., 2016, 2018). The foreshock is a region magnetically connected to the bow shock (Greenstadt et al., 1980; Eastman et al., 1981; Hao YF et al., 2023a, b) and is filled with backstreaming particles, which provide free energy to create waves or excite instabilities (Sentman et al., 1983; Tanaka et al., 1983; Archer et al., 2005; Shan LC et al., 2018; Hao YF et al., 2023c). Both the terrestrial and Martian foreshocks are suggested to be sources of the sub-ion-scale magnetic holes, based on their occurrence rate in the upstream region of the terrestrial and Martian bow shocks (Wang GQ et al., 2020c, 2021a).

Mercury, the closest planet to the Sun, has a global intrinsic magnetic field (Diego et al., 2020; Jarvinen et al., 2020). The magnetic holes with durations of >1 s have been statistically studied based on observations by the MESSENGER (MErcury Surface, Space ENvironment, GEochemistry, and Ranging) spacecraft (Volwerk et al., 2020; Karlsson et al., 2021). Their sizes follow a log-normal distribution (Karlsson et al., 2021), and their occurrence rate is ~3.4 per day (Volwerk et al., 2020). Karlsson et al. (2021) further found that their ambient magnetic field strength is generally lower than the average interplanetary magnetic field (IMF) strength, indicating that they might be more likely to occur in the high-β region. The authors also found that the properties of the magnetic holes in Mercury's magnetosheath are similar to those in the solar wind; thus, they argued that the magnetic holes in the magnetosheath have a solar wind origin.

In this study, we statistically investigate the magnetic holes in the solar wind at Mercury's orbit based on observations by the MESSENGER spacecraft. We show that a new group of magnetic holes with durations of 0.1–0.6 s exist in the upstream region of Mercury's bow shock.

2. Observation

2.1 Selection of Magnetic Holes

The MESSENGER spacecraft, launched on August 3, 2004, was inserted into a high-eccentricity and ~80° inclination orbit around Mercury in March 2011 (Solomon et al., 2007). In the present study, we use the magnetic field data sampled at 20 Hz (i.e., with a time resolution of 0.05 s) measured by the magnetometer instrument (Anderson et al., 2007) from January 1 to December 31, 2012, to investigate the magnetic holes in the solar wind at Mercury's orbit. Philpott et al. (2020) have provided Mercury's magnetopause crossings and bow shock crossings for the MESSENGER spacecraft based on the procedure outlined by Winslow et al. (2013). We obtain the time intervals in the solar wind from Mercury's bow shock crossings listed in the Supplement of Philpott et al. (2020). In total, 221.6 days of data in the solar wind are available. Figure 1 shows the orbit coverage of the MESSENGER spacecraft in the X–Y and X–Z planes in the Mercury solar orbital (MSO) coordinate system. The color denotes the dwell time of MESSENGER in each grid with a grid size of 0.2 R_M (Mercury radius). Figure 1a shows that the data at $Y_{MSO} < 0$ is more than that at $Y_{MSO} > 0$. Figure 1b shows that the orbit coverage of the MESSENGER spacecraft is mainly at $Z_{MSO} < 0$.

The selection of magnetic holes generally requires consideration of the ambient magnetic field (Zhang TL et al., 2008; Sun WJ et al., 2012). Because the duration of the magnetic hole in the solar wind has a wide range of values from <1 s to tens of seconds (Zhang TL et al., 2008; Wang GQ et al., 2021c) and the IMF is time variant, the magnetic field data low-pass filtered with the same cut-off frequency is no longer reasonable as the ambient magnetic field. In other words, it is difficult to identify both the small and large durations of the magnetic holes in the solar wind when using the same temporal window. Therefore, we use different cut-off frequencies to obtain the ambient magnetic field to select the magnetic holes with different ranges of durations.

We set temporal windows of 2, 10, 60, and 300 s to select the magnetic holes with a duration of 0–1 s, 1–5 s, 5–30 s, and 30–150 s, respectively. We first search out the local minima of the magnetic field strength $|\boldsymbol{B}|$. For each minimum $|\boldsymbol{B}|$ at T_0, the starting and ending times of the temporal window are set to be $T_0 - 0.5T_{win}$ and $T_0 + 0.5T_{win}$, respectively, where T_{win} is 2, 10, 60, or 300 s. We then determine the time of the boundary for each event by using the method of Wang GQ et al. (2021c). For a given temporal window T_{win}, we can obtain the ambient magnetic field strength B_{sm} and the standard deviation σ of $|\boldsymbol{B}| - B_{sm}$, where B_{sm} is the $|\boldsymbol{B}|$ smoothed with a temporal window of T_{win}. We select the time with $|\boldsymbol{B}| = B_{sm} + 0.5\sigma$ closest to T_0 from the left (right) as the time of the left (right) boundary of the potential magnetic hole. If the times of the left and right boundaries are not found simultaneously, we then select the time with $|\boldsymbol{B}| = B_{sm}$ and $|\boldsymbol{B}| = B_{sm} - 0.5\sigma$ as the second and third choices to find the times of the left and right boundaries, respectively. Figure 2 shows an example of the selection of the magnetic holes with a minimum $|\boldsymbol{B}|$ at 08:58:55.6 universal time (UT) on March 2, 2012. The use of the $|\boldsymbol{B}|$ smoothed with a 2-s boxcar filter as the ambient magnetic field is suitable for this event. And the times where $|\boldsymbol{B}| = B_{sm} + 0.5\sigma$ closest to 08:58:55.6 UT are selected as the boundary times of this magnetic hole.

After obtaining the time of the boundaries, the potential magnetic hole is required to meet the following criteria: (1) $B_{min}/B_{edge} < 0.85$, where B_{min} is the minimum $|\boldsymbol{B}|$ between the

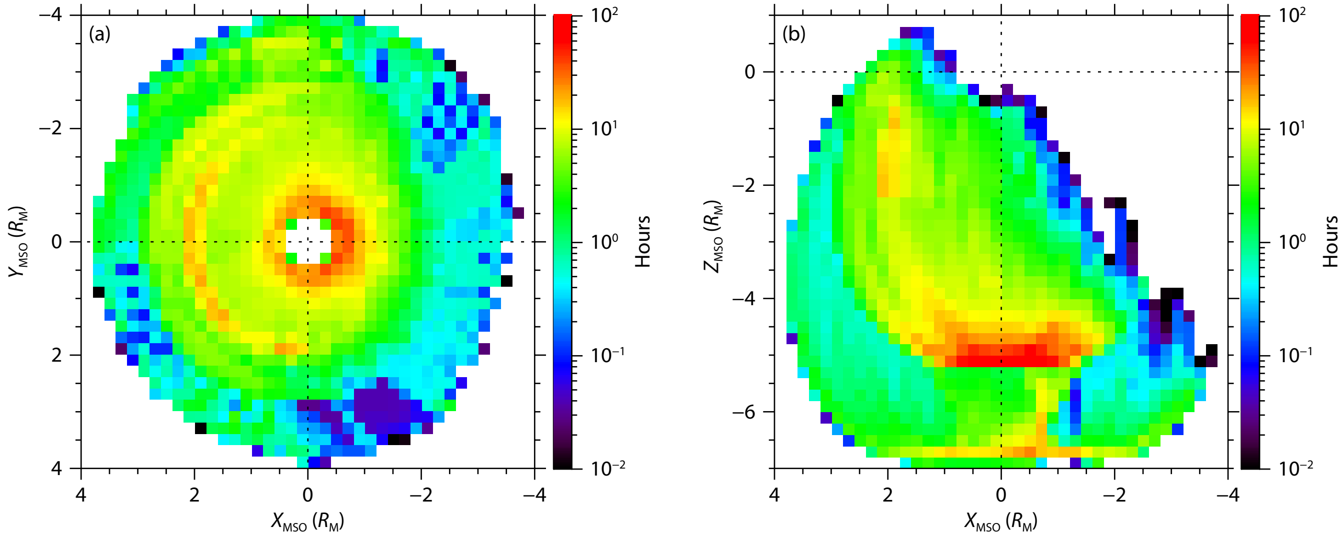

Figure 1. Orbit coverage of the MESSENGER spacecraft in the solar wind in the X_{MSO}–Y_{MSO} (a) and X_{MSO}–Z_{MSO} (b) planes from January 1 to December 31, 2012. The grid size is 0.2 R_M.

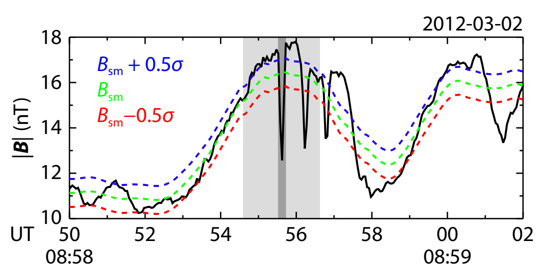

Figure 2. An example of the selection of magnetic holes. B_{sm} is the |$\boldsymbol{B}$| smoothed with a 2-s boxcar filter, and σ is the standard deviation of |$\boldsymbol{B}$| – B_{sm} between 08:58:54.6 and 08:58:56.6 UT on March 2, 2012. The black curve denotes |$\boldsymbol{B}$|. The blue, green, and red dashed lines denote $B_{sm} + 0.5\sigma$, B_{sm}, and $B_{sm} - 0.5\sigma$, respectively.

two boundaries of the event, and B_{edge} is the average |$\boldsymbol{B}$| at the two boundaries; (2) $B_{edge} - B_{min} > 0.5$ nT; (3) $\omega < 15°$, where ω is the angle between the magnetic field vectors at the two boundaries. The value 0.5 nT of the criterion $B_{edge} - B_{min}$ is an empirical value to reduce the effect of the magnetic field noise, such as the variable spacecraft field (Anderson et al., 2007). We visually check all the automatically selected events to select the unambiguous magnetic holes. Finally, 2656 magnetic holes are selected for 1 year of MESSENGER observations.

2.2 Durations and B_{min}/B_{edge} of Magnetic Holes

Figure 3 shows histograms of the durations of our selected magnetic holes, which can be clearly divided into two groups: 0.1–0.6 s (orange) and 0.6–100 s (blue). We classify the 757 magnetic holes with durations of <0.6 s and 1899 magnetic holes with durations of >0.6 s as the small and large durations of the magnetic holes (abbreviated as SDMHs and LDMHs), respectively. The durations of the LDMHs approximately obey a log-normal distribution, expressed by

$$f(\lg(x)) = \frac{1}{\sqrt{2\pi}\sigma}\exp\left(-\frac{(\lg(x)-\mu)^2}{2\sigma^2}\right),$$

where x denotes the duration of the magnetic hole, σ is the standard deviation, and μ is the median of the log-normal distribution. For the SDMHs, their durations roughly obey a log-normal distribution, but not convincingly. One possible reason is that the resolution of the magnetic field data at 20 Hz is not high enough, leading to a gap between some adjacent orange histograms, as shown in Figure 3. For the SDMHs and LDMHs, μ is –0.61 and 0.48, respectively. Thus, the median durations of the SDMHs and LDMHs are expected to be ~0.25 and 3 s, respectively.

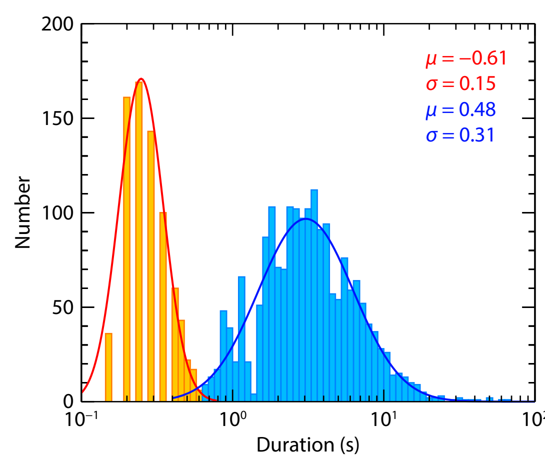

Figure 3. Histograms of the durations of the SDMHs (orange) and LDMHs (blue). The red and blue curves denote the fitted log-normal distributions for the orange and blue histograms, respectively. The corresponding median μ and standard deviation σ of the fitted log-normal distribution are also given. The median duration of the magnetic holes for the orange distribution is approximately 0.25 s and that for the blue distribution is approximately 3 s.

Figure 4a shows the histograms of B_{min}/B_{edge} for the SDMHs (orange) and LDMHs (blue). The B_{min}/B_{edge} is >0.5 for 98.3% of the SDMHs, and the proportion of the magnetic holes tends to be larger when B_{min}/B_{edge} increases from 0.5 to 0.85. For the LDMHs, 32.6% of the magnetic holes have a B_{min}/B_{edge} value of <0.5, and their proportion tends to gradually increase with the increase in

B_{min}/B_{edge} from 0 to 0.85. Figure 4b shows that the values of $B_{edge} - B_{min}$ for 256 (425) out of 757 SDMHs are in the range of 1–2 (2–4) nT. The values of $B_{edge} - B_{min}$ are much larger for the LDMHs than the SDMHs overall.

2.3 Polarization

The minimum variance analysis (MVA; Sonnerup and Scheible, 1998) can be used to investigate the polarization of waves or magnetic holes (e.g., Sonnerup and Cahill, 1967; Balikhin et al., 2012). We transform the magnetic field from the MSO into the LMN coordinate system by MVA using the data during each magnetic hole, where the *L*, *M*, and *N* axes denote the maximum, intermediate, and minimum variance directions, respectively; the three eigenvalues are λ_1, λ_2, and λ_3. If λ_2 and λ_3 are small in

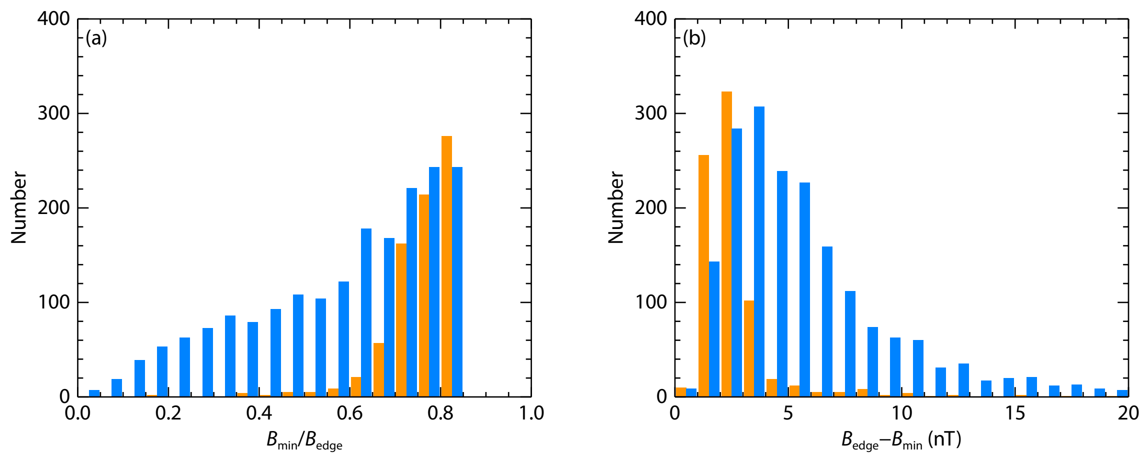

Figure 4. Histograms of B_{min}/B_{edge} (a) and $B_{edge} - B_{min}$ (b) for the SDMHs (orange) and LDMHs (blue). B_{edge} is the average |***B***| at the two boundaries of the magnetic hole, and B_{min} is the minimum |***B***| inside the magnetic hole.

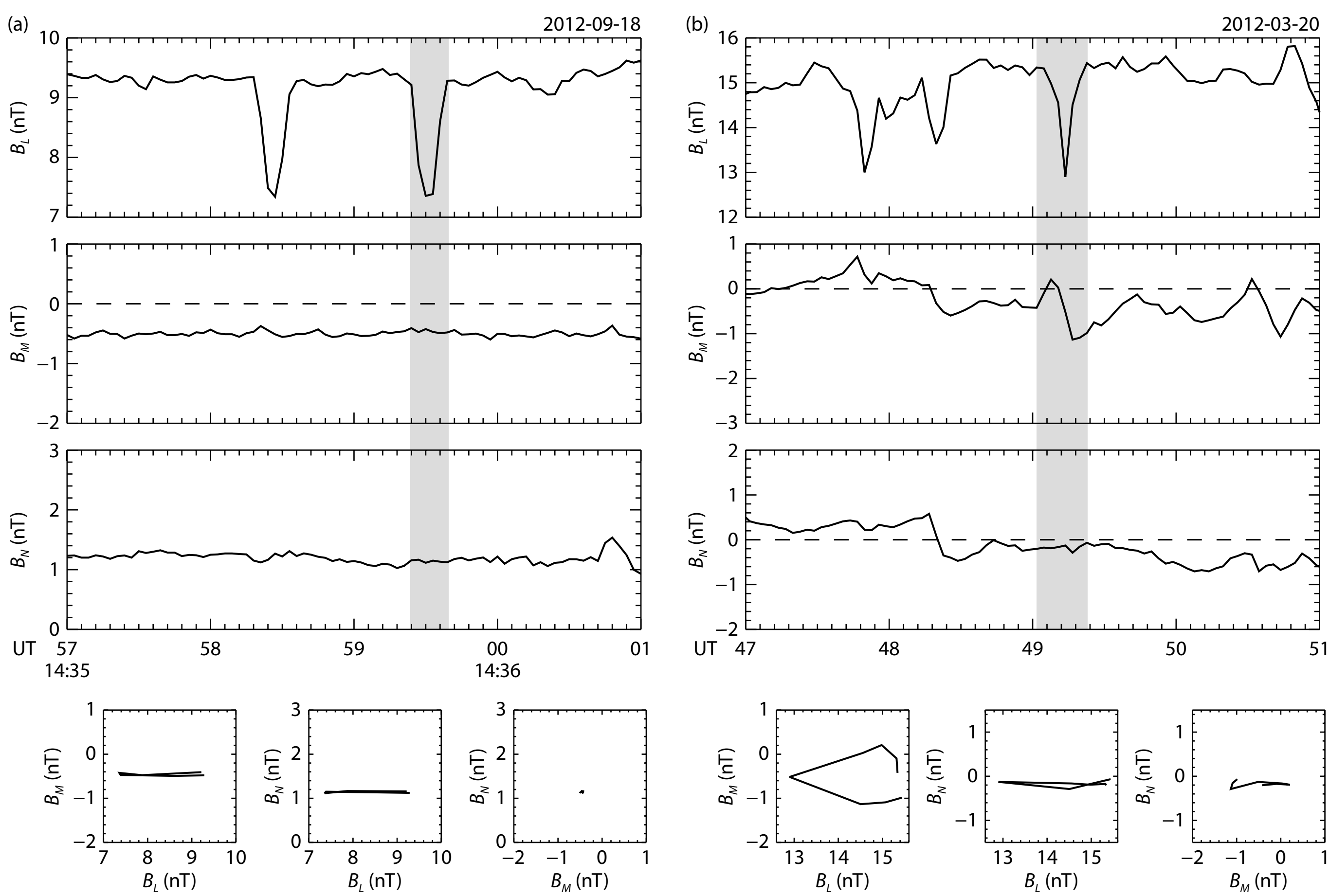

Figure 5. The magnetic field in *LMN* and the plots of B_M versus B_L, B_N versus B_L, and B_N versus B_M during the magnetic hole between 14:35:59.4 and 14:35:59.65 UT on September 18, 2012 (a) and between 20:52:49.02 and 20:52:49.38 UT on March 20, 2012 (b).

comparison to λ_1 and are close to each other, the polarization is linear (e.g., Balikhin et al., 2012).

Figure 5a shows a SDMH between 14:35:59.4 and 14:35:59.65 UT on September 18, 2012. During this structure, B_L shows a decrease of ~2 nT, whereas B_M and B_N show little change. For this magnetic hole, λ_1, λ_2, and λ_3 are 5.54, 0.0588, and 0.0459 nT^2, respectively, and λ_1/λ_2 is ~94, much larger than 1. The bottom panels in Figure 5a show the plots of B_M versus B_L, B_N versus B_L, and B_N versus B_M during the magnetic hole, which illustrates that this structure has linear polarization. Figure 5b shows another SDMH between 20:52:49.02 and 20:52:49.38 UT on March 20, 2012. Its three eigenvalues are 0.604, 0.241, and 0.00358 nT^2, respectively. In contrast to the SDMH in Figure 5a, this SDMH has a bipolar variation of B_M. The plot of B_M versus B_L indicates that this SDMH has elliptical polarization.

Figure 6a shows a LDMH with a duration of ~14 s observed at ~11:04:15 UT on August 7, 2012. Its duration is much larger than that of the magnetic hole (~0.3 s) in Figure 5. The magnetic field depression is mainly in B_L during the magnetic hole, whereas B_M and B_N have high-frequency fluctuations with an amplitude of <1 nT. The eigenvalues λ_1, λ_2, and λ_3 are 5.55, 0.059, and 0.046 nT^2, respectively. And the plots of B_M versus B_L, B_N versus B_L, and B_N versus B_M during this magnetic hole indicate that this structure has linear or quasi-linear polarization, although λ_2 is not small enough in comparison to λ_1. Figure 6b shows another LDMH with a duration of ~2.7 s, for which λ_1/λ_2 is ~6.76. In contrast to the LDMH in Figure 6a, B_M shows a significant change, with a temporal scale of 10 s. The plot of B_M versus B_L indicates that this structure has elliptical polarization.

Figures 7a and 7b show the distributions of the magnetic holes with different values of λ_1/λ_2 and λ_2/λ_3 for the SDMHs and LDMHs. For each magnetic hole, the eigenvalues are determined by MVA using the magnetic field data for the entire interval of this magnetic hole. For the SDMHs, 38.3% of the magnetic holes have λ_2/λ_3 < 10. In contrast, Figure 7b shows that 79.8% of the LDMHs have λ_2/λ_3 < 10. The medians of λ_2/λ_3 are ~14.7 and 4.3 for the SDMHs and LDMHs, respectively. Approximately 8.9% (3.4%) of λ_1/λ_2 is in the range of 1–5 for the SDMHs (LDMHs), and ~17.8% (12.4%) of λ_1/λ_2 is in the range of 5–10. This indicates that the polarization of both SDMHs and LDMHs can be elliptical, quasi-linear, or linear. The distribution of λ_2/λ_3 for the SDMHs is clearly different from that of the LDMHs, as shown in Figures 7c and 7d. Such a large difference may have been overestimated because the sampling points can affect the accuracy of MVA (Khrabrov and Sonnerup, 1998).

2.4 Occurrence Rate

Figure 8a shows the orbit coverage of the MESSENGER spacecraft in the solar wind during the time intervals we used in the X–R_{YZ} plane, where $R_{YZ} = \sqrt{Y_{\rm MSO}^2 + Z_{\rm MSO}^2}$. The grid size is 0.5 $R_{\rm M}$. We require

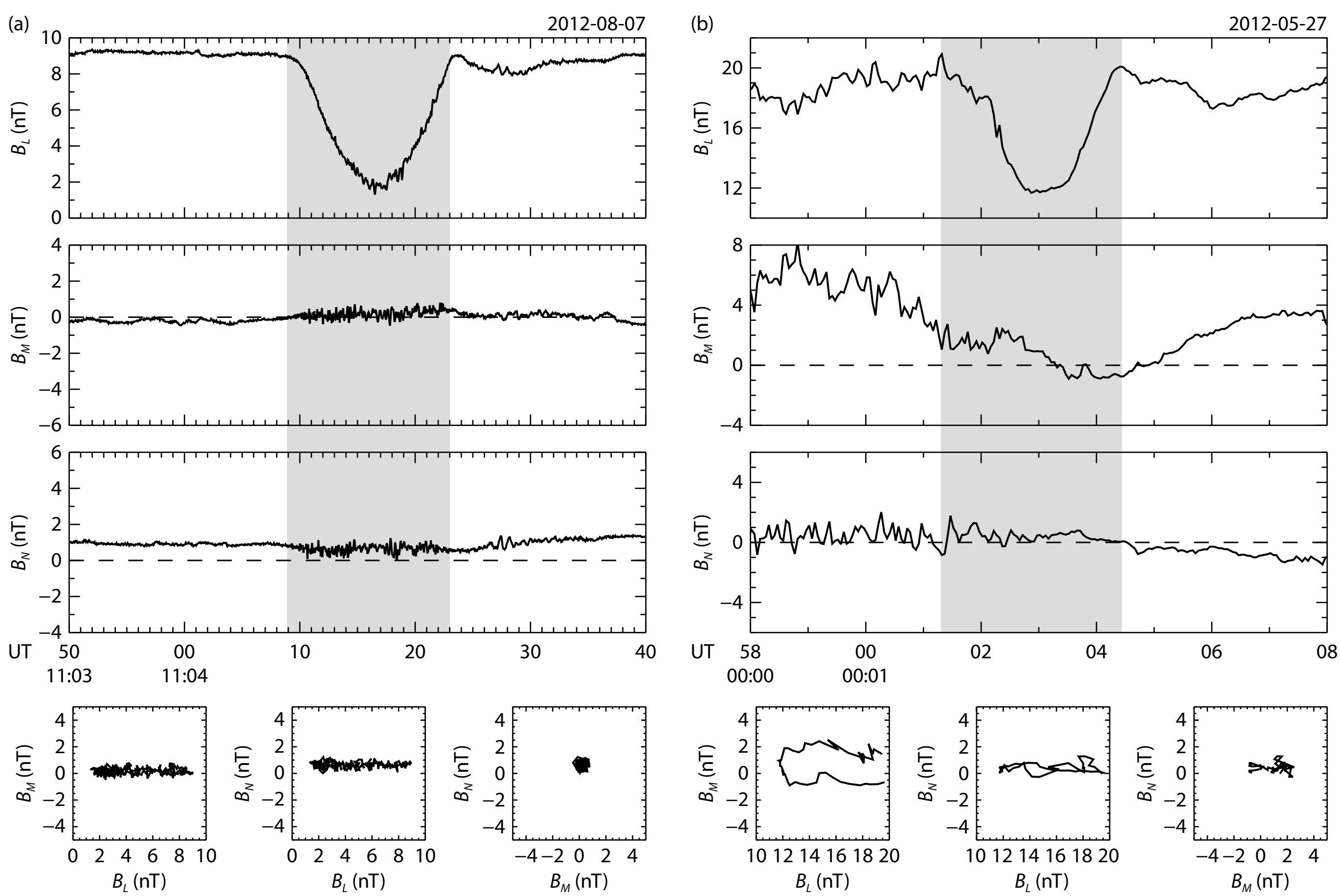

Figure 6. The magnetic field in LMN and the plots of B_M versus B_L, B_N versus B_L, and B_N versus B_M during the magnetic hole between 11:04:09 and 11:04:23 UT on August 7, 2012 (a) and between 00:01:01.61 and 00:01:04.27 UT on May 27, 2012 (b).

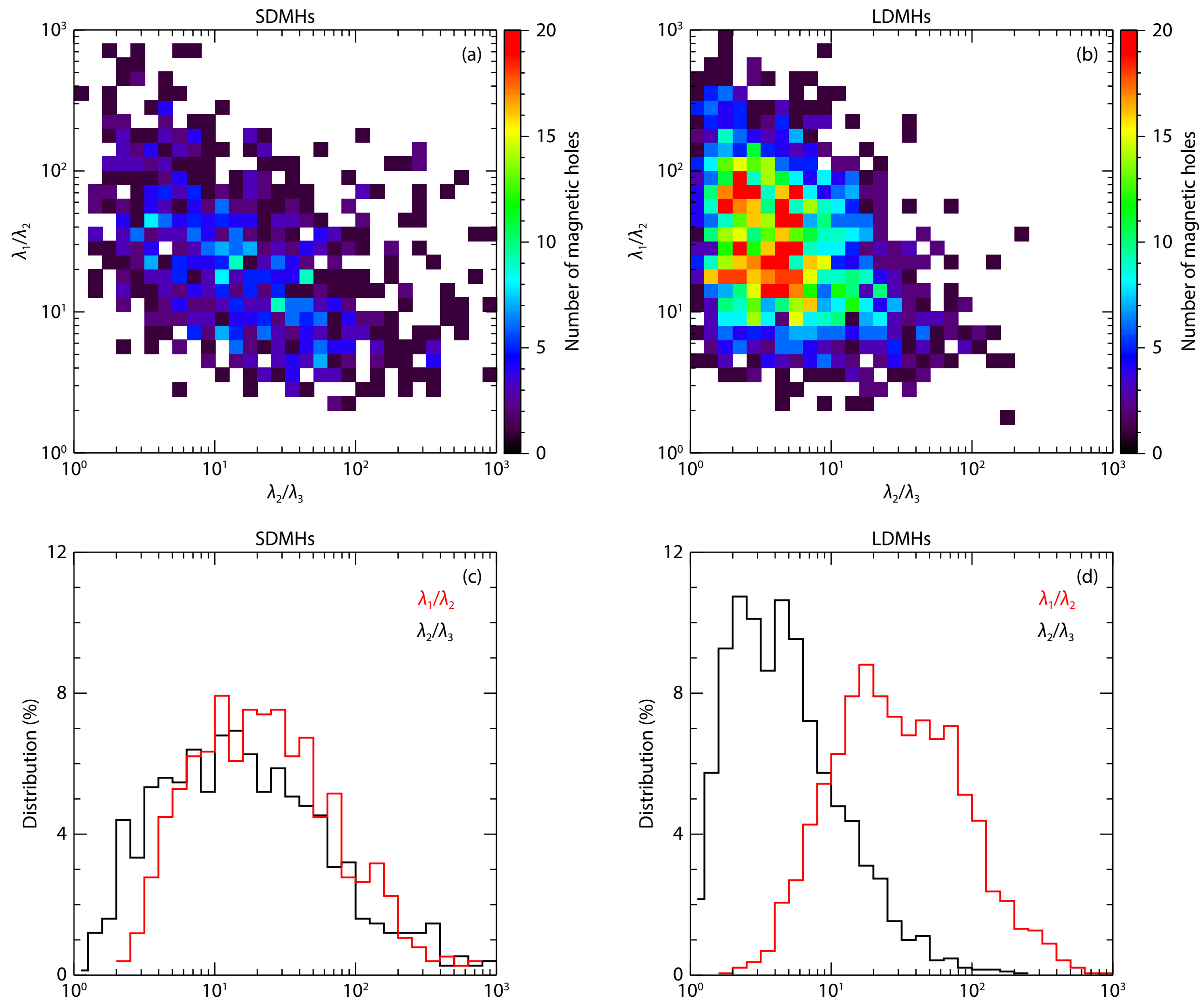

Figure 7. Distributions of the number of magnetic holes with different values of λ_1/λ_2 and λ_2/λ_3 for the SDMHs (a) and LDMHs (b), respectively. Histograms of λ_1/λ_2 (red) and λ_2/λ_3 (black) for the SDMHs (c) and LDMHs (d), respectively.

the amount of data in each grid to be at least 5 h. The average bow shock position under a solar wind ramp pressure of 14.3 nPa (Winslow et al., 2013) is also given in Figure 8. The bow shock boundary changes with the variation in the solar wind ramp pressure as well as the Alfvén Mach number. For example, its subsolar standoff distance varies from 2.29 to 1.89 R_M when the Alfvén Mach number changes from 4.12 to 11.8 (Winslow et al., 2013). Nevertheless, the bow shock shape remains unchanged when the solar wind ramp pressure or the Alfvén Mach number changes (Winslow et al., 2013).

Magnetic holes are often observed successively within several minutes, and some are observed in isolation during a long period (see Zhang TL et al., 2008). Here, two adjacent magnetic holes in each group are considered to belong to the same train of magnetic holes if they are observed within 300 s (see Zhang TL et al., 2008). A single magnetic hole or a train of magnetic holes is regarded as a magnetic hole event, and we focus on the occurrence rate of the magnetic hole event instead of each single magnetic hole. In total, we obtain 160 SDMH and 862 LDMH events, respectively. The average position during the entire event is considered the position of this event. Figure 8b shows the occurrence rates of the SDMH events in the X–R_{YZ} plane. The black grid indicates that no events are observed in the corresponding region. The occurrence rates are mainly in the range of 0.3–5.5 events per day, and they tend to be larger when closer to the bow shock. Figure 8c shows the occurrence rates of the LDMH events in the X–R_{YZ} plane, which are mainly in the range of 0.6–16.6 events per day. Several local maxima of the occurrence rates generally occur at the bins with <10 h of data. Except for these local maxima, the distribution of the occurrence rates is approximately uniform.

To check whether Mercury's foreshock can affect the occurrence of the magnetic hole events, we attempt to determine the relation between the direction of the magnetic field line and the occurrence of the magnetic hole events. For the same magnetic field line, the direction of the magnetic field vector $\boldsymbol{B}$ has two possibilities. Thus, we set $\boldsymbol{B}_1$ (= $[B_{X1}, B_{Y1}, B_{Z1}]$) = $\boldsymbol{B}$ if the X_{MSO} component of $\boldsymbol{B}$ is positive, otherwise $\boldsymbol{B}_1 = 0 - \boldsymbol{B}$. An abundance of waves are in the frequency range of 0.1–4 Hz in the foreshock (Jarvinen et al., 2020; Romanelli et al., 2020). To reduce the effect of these high-frequency waves, the magnetic field data have been smoothed

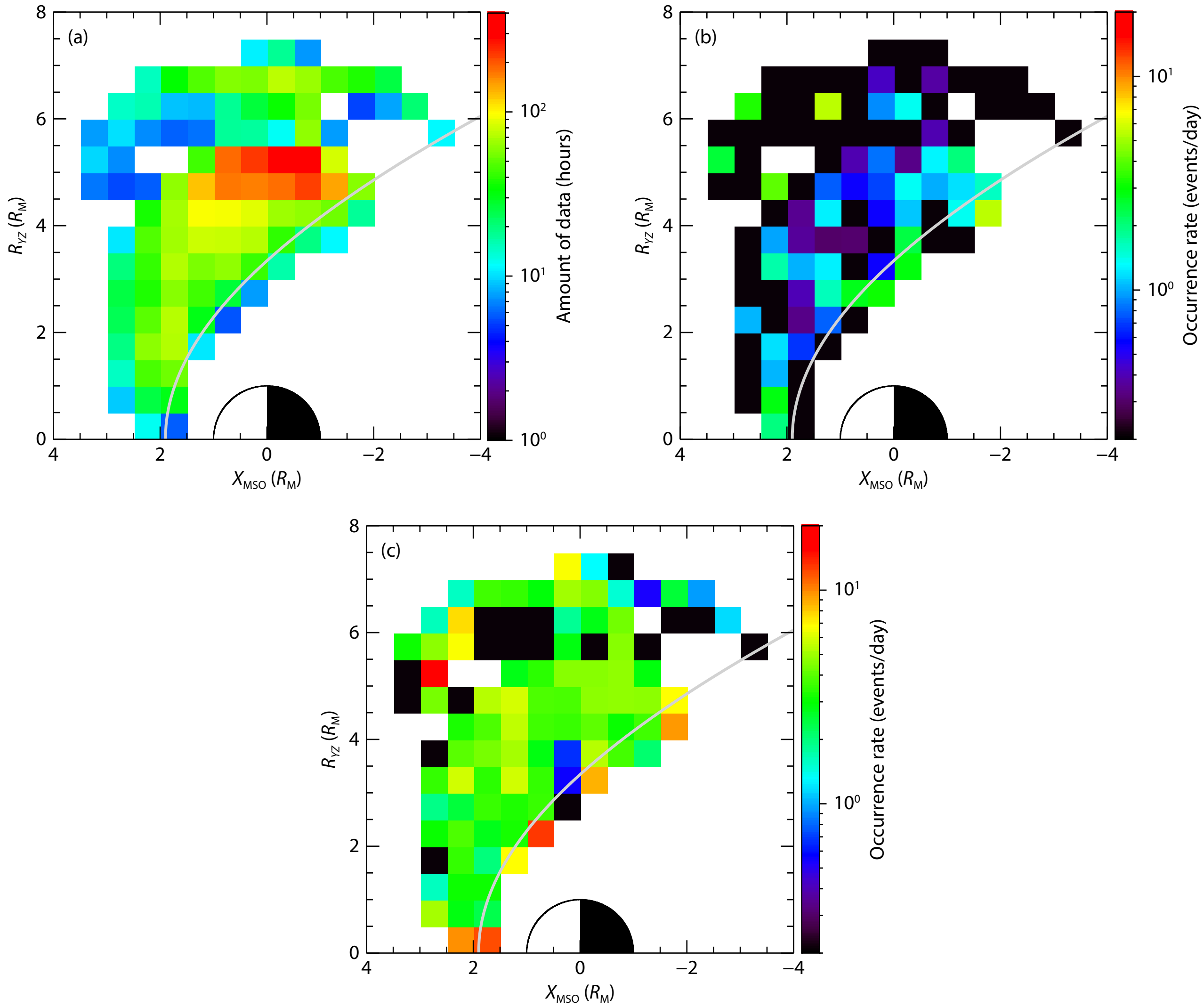

Figure 8. Orbit coverage of the MESSENGER spacecraft (a) and the occurrence rates of the SDMH (b) and LDMH (c) events in the upstream region of Mercury's bow shock in the X–R_{YZ} plane. The gray curve denotes the average bow shock position under a solar wind ramp pressure of 14.3 nPa, as determined by the model of Winslow et al. (2013).

with a 20-s boxcar filter before determining the IMF direction.

Figure 9a shows the amount of data in the magnetic field we used at different θ and ϕ for the data measured by MESSENGER at $Y_{MSO} < -1$ R_M, where

$$\theta = \frac{\pi}{2} - \arctan(B_{Y1}/B_{X1}),$$

and

$$\phi = \arctan(B_{Z1}/\sqrt{B_{X1}^2 + B_{Y1}^2}).$$

Here, $\theta = 0$ (180°) and $\phi = 0$ indicate that the magnetic field vector points to the positive (negative) Y axis. The step lengths of both θ and ϕ are 45°. The distribution of the amount of data is symmetrical with respect to $\phi = 0$. The maximum value is at $90° < \theta < 135°$ and $-45° < \phi < 45°$, which meets the expectation of the Parker spiral configuration (Meyer-Vernet, 2007; Chang et al., 2019). Figure 9b shows the distribution of the magnetic field data in the θ–ϕ plane for the data measured at $Y_{MSO} > 1$ R_M, whose characteristics are the same as those in Figure 9a except that the overall amount of data in each grid in Figure 9b is relatively smaller.

Forty-eight and 17 SDMH events are observed at $Y_{MSO} < -1$ R_M and $Y_{MSO} > 1$ R_M, respectively. Figure 10a shows the occurrence rate of the SDMH events at $Y_{MSO} < -1$ R_M in the θ–ϕ plane. The occurrence rate is ~1.92 events per day in the bin with $90° < \theta < 135°$ and $-45° < \phi < 0°$, much larger than that of other bins with a value of ~0.26–1.1 events per day. In contrast, Figure 10b shows that the maximum occurrence rate (~2.03 events per day) is in the bin with $45° < \theta < 90°$ and $-45° < \phi < 0°$, and it is much larger than that in other bins, with a value of 0–0.58 events per day. At $Y_{MSO} < -1$ ($Y_{MSO} > 1$) R_M, the spacecraft has a higher probability of being located in the foreshock when $\phi < 0$ and $90° < \theta < 135°$ ($45° < \theta < 90°$) than that when $\phi < 0$ and other values of θ. This result suggests that the SDMH events are more likely to be observed in Mercury's foreshock. Contrary to the SDMH events, Figure 10c show that the occurrence rate is the minimum at $90° < \theta < 135°$ and $-45° < \phi < 0°$, suggesting that the LDMH events have a smaller occurrence rate in Mercury's foreshock.

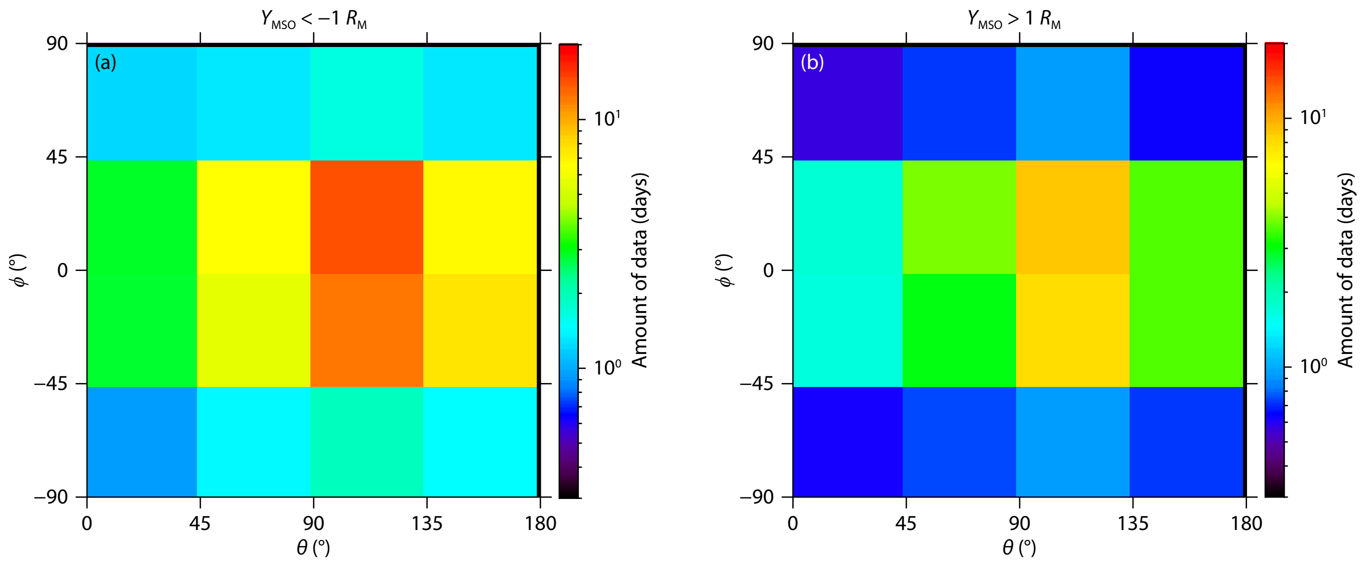

Figure 9. The distribution of the magnetic field data at $Y_{MSO} < -1\ R_M$ (a) and $Y_{MSO} > 1\ R_M$ (b) in the θ–ϕ plane.

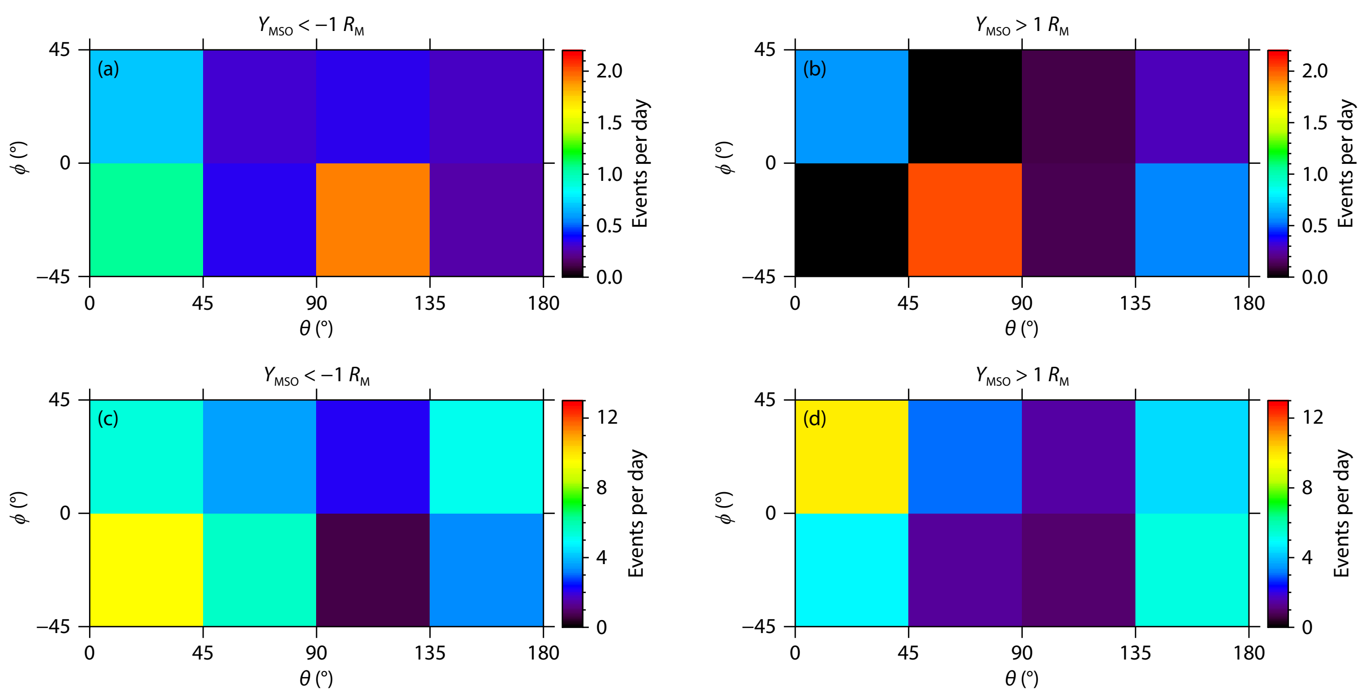

Figure 10. (a, b) Occurrence rates of the SDMH events observed at $Y_{MSO} < -1\ R_M$ and $Y_{MSO} > 1\ R_M$ in the θ–ϕ plane. (c, d) Occurrence rates of the LDMH events observed at $Y_{MSO} < -1\ R_M$ and $Y_{MSO} > 1\ R_M$ in the θ–ϕ plane.

In the solar wind at Mercury's orbit, the magnetic holes with durations of >1 s are more likely to be observed when the IMF $|\boldsymbol{B}|$ is lower than the average strength (Karlsson et al., 2021), indicating that the IMF $|\boldsymbol{B}|$ might affect the occurrence of these magnetic holes. Figure 11a shows the amount of magnetic field data at different IMF $|\boldsymbol{B}|$ with a step length of ΔB = 2 nT. We require the amount of data in each bin to be at least 1 d. If the duration of an event is >6 min, the average $|\boldsymbol{B}|$ during this event is considered the ambient magnetic field strength. Otherwise, the average $|\boldsymbol{B}|$ during the interval 3 min before and after the central moment of this event is considered the ambient magnetic field strength of the magnetic hole event. Figure 11b shows the occurrence rates of the SDMH (blue) and LDMH (orange) events. For both groups, the occurrence rates tend to decrease with an increase in $|\boldsymbol{B}|$ until it is ~16 nT, and they are small when $|\boldsymbol{B}|$ > 16 nT, suggesting that the magnetic hole events in both groups are more likely to be observed when the IMF $|\boldsymbol{B}|$ is weak compared with the average IMF $|\boldsymbol{B}|$.

3. Discussion

An abundance of magnetic holes are in the solar wind at Mercury's orbit (Russell et al., 2008; Volwerk et al., 2020; Karlsson et al., 2021). On the basis of MESSENGER data, Volwerk et al. (2020) and Karlsson et al. (2021) statistically studied the properties of

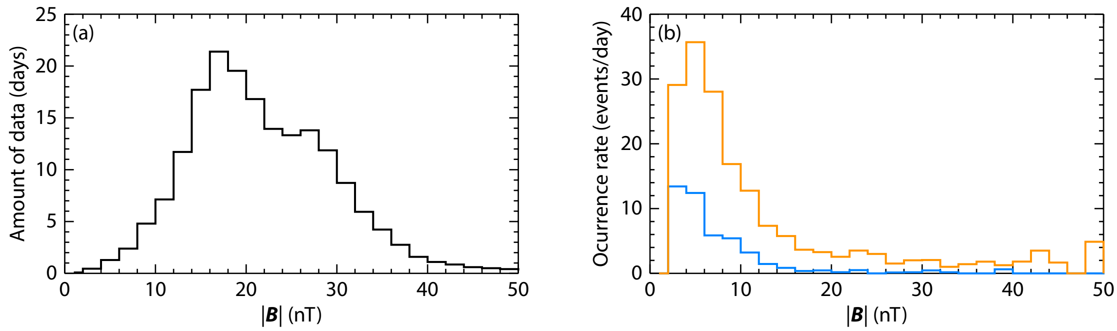

Figure 11. (a) Amount of magnetic field data in the solar wind we used at different IMF |***B***| with a step length of ΔB = 2 nT. (b) Occurrence rates of the SDMH (blue) and LDMH (orange) events at different IMF |***B***|.

these magnetic holes with durations of >1 s. However, the short-duration (<1 s) magnetic holes have not attracted much attention. We analyze the properties of the magnetic holes with durations of 0.1–100 s in the upstream region of Mercury's bow shock. We find it interesting that these magnetic holes can be divided into two groups according to the distribution of their durations (see Figure 3). The SDMHs and LDMHs have a duration of 0.1–0.6 s and 0.6–100 s, respectively. One must note that there is no clear boundary between the durations of the SDMHs and LDMHs, as shown in Figure 3. Such a distribution of the magnetic holes is similar to that upstream of the Martian bow shock (Wang GQ et al., 2021c). Wang GQ et al. (2021c) found that the group of magnetic holes with small durations are sub-ion scale. We speculate that the SDMHs are also sub-ion scale, and the observational duration of 0.6 s might be the boundary between typical sub-ion- and ion-scale magnetic holes.

In the solar wind at Mars' orbit, the group of magnetic holes with large (small) durations is suggested to be ion (sub-ion) scale (Wang GQ et al., 2021c). Unfortunately, we are unable to determine the sizes of our selected SDMHs and LDMHs because of the lack of plasma data. The SDMHs and LDMHs show some different properties, such as the distributions of B_{min}/B_{edge} and λ_2/λ_3. In contrast to the previous observations in the solar wind at Mercury's orbit, our results suggest that the SDMHs are a new group of magnetic holes.

We use 221.6 d of the data in the solar wind to select 160 SDMH events and 862 LDMH events, respectively. The average occurrence rates are ~0.72 and 3.89 events per day for the SDMH and LDMH events, respectively. This result suggests that the occurrence rate of the LDMH events is much larger than that of the SDMH events. For the SDMH events, the maximum occurrence rate occurs when 90° < θ < 135° and −45° < ϕ < 0° at Y_{MSO} < −1 R_M, and it occurs when 45° < θ < 90° and −45° < ϕ < 0° at Y_{MSO} > 1 R_M. As shown in Figures 10a and 10b, both maximum occurrence rates are much larger than the values in other bins. Considering the orbit of the MESSENGER spacecraft, the IMF with 90° < θ < 135° (45° < θ < 90) and −45° < ϕ < 0° might have a higher probability of being connected to the bow shock than other bins when the spacecraft is at Y_{MSO} < −1 (Y_{MSO} > 1) R_M. This suggests that the SDMH events are more likely to be observed in Mercury's foreshock. In contrast, the occurrence rate in Figures 10c is minimum at the bins where the occurrence rate is maximum for the SDMH events. We speculate that the LDMHs originate from the upstream solar wind and that the foreshock can destroy some of these magnetic holes, leading to the decrease in their occurrence rate in the foreshock.

The occurrence rates of the magnetic hole events in both groups are significantly affected by the IMF strength (see Figure 11). The lower the magnetic field intensity, the higher the occurrence rate of the magnetic hole event. This finding indicates that the magnetic holes in both groups are more likely to occur in the high-β plasma, which is consistent with the findings of Karlsson et al. (2021). Thus, mirror instabilities are a potential generation mechanism of these magnetic holes, or the mirror unstable condition contributes to their formation. The foreshock has different impacts on the occurrence rate of the SDMH and LDMH events. If the foreshock is one source of the SDMHs, the plasma in Mercury's foreshock might provide some clues that would reveal their generation mechanism, which needs study in the future.

4. Summary

We investigate magnetic holes with durations of 0.1–100 s in the upstream region of Mercury's bow shock by using the magnetic field data from the MESSENGER spacecraft from January 1 to December 31, 2012. According to the distributions of their durations, the magnetic holes can be divided into two groups: smaller and larger than 0.6 s. The durations of both groups approximately obey a log-normal distribution, with a median of ~0.25 s and 3 s, respectively. Both groups have linear, quasi-linear, or elliptical polarization. Approximately 1.7% and 32.6% of the magnetic holes have a value of B_{min}/B_{edge} < 0.5 for the SDMHs and LDMHs, respectively. In addition, these two groups have different distributions of λ_2/λ_3, with a median of ~14.7 and 4.3 for the SDMHs and LDMHs, respectively.

For both groups, their occurrence rates tend to be smaller when the IMF strength is stronger until the IMF strength is up to 16 nT, and they are small when the IMF strength is >16 nT, indicating that they prefer to occur in the high-β plasma. The SDMH events have a much larger occurrence rate when the IMF has a higher probability of being connected to the bow shock, suggesting that Mercury's foreshock might be a source of these magnetic holes. In contrast, the LDMH events have a smaller occurrence rate when the IMF has a higher probability of being connected to the bow shock, suggesting that some LDMHs could be destroyed in Mercury's foreshock.

Acknowledgments

This work was supported by the Fundamental Research Funds for the Central Universities (Grant No. HIT.OCEF.2022041), the National Natural Science Foundation of China (Grant Nos. 42241155, 41974205, 42130204, and 42241133), the Guangdong Basic and Applied Basic Research Foundation (Grant Nos. 2022A1515011698, 2023A1515030132, and 2022A1515010257), the Shenzhen Science and Technology Research Program (Grant Nos. JCYJ20210324121412034 and JCYJ20210324121403009), the Shenzhen Key Laboratory Launching Project (Grant No. ZDSYS20210702140800001), the Joint Open Fund of Mengcheng National Geophysical Observatory (Grant No. MENGO-202315), the Macau Foundation, the pre-research Project on Civil Aerospace Technologies (Grant No. D020103) funded by the China National Space Administration, and the Chinese Academy of Sciences Center for Excellence in Comparative Planetology. We acknowledge the entire MESSENGER team for providing the data.

Data Availability

The data from the MESSENGER spacecraft are publicly available from the Planetary Data System (https://pds-ppi.igpp.ucla.edu/search/?sc=Messenger&facet=SPACEC RAFT_NAME).

References

Anderson, B. J., Acuña, M. H., Lohr, D. A., Scheifele, J., Raval, A., Korth, H., and Slavin, J. A. (2007). The magnetometer instrument on MESSENGER. *Space Sci. Rev.*, *131*(1-4), 417–450. https://doi.org/10.1007/s11214-007-9246-7

Archer, M., Horbury, T. S., Lucek, E. A., Mazelle, C., Balogh, A., and Dandouras, I. (2005). Size and shape of ULF waves in the terrestrial foreshock. *J. Geophys. Res.: Space Phys.*, *110*(A5), A05208. https://doi.org/10.1029/2004ja010791

Balikhin, M. A., Sagdeev, R. Z., Walker, S. N., Pokhotelov, O. A., Sibeck, D. G., Beloff, N., and Dudnikova, G. (2009). THEMIS observations of mirror structures: magnetic holes and instability threshold. *Geophys. Res. Lett.*, *36*(3), L03105. https://doi.org/10.1029/2008gl036923

Balikhin, M. A., Sibeck, D. G., Runov, A., and Walker, S. N. (2012). Magnetic holes in the vicinity of dipolarization fronts: mirror or tearing structures?. *J. Geophys. Res.: Space Phys.*, *117*(A8), A08229. https://doi.org/10.1029/2012ja017552

Chang, Q., Xu, X. J., Xu, Q., Zhong, J., Xu, J. Y., Wang, J., and Zhang, T. L. (2019). Multiple-point modeling the Parker spiral configuration of the solar wind magnetic field at the solar maximum of Solar Cycle 24. *Astrophys. J.*, *884*(2), 102. https://doi.org/10.3847/1538-4357/ab412a

Chen, Y. J., Wu, M. Y., Xiao, S. D., Du, A. M., Wang, G. Q., Chen, Y. Q., Pan, Z. H., and Zhang, T. L. (2022). Magnetic fluctuations associated with small-scale magnetic holes in the Martian magnetosheath. *Front. Astron. Space Sci.*, *9*, 858300. https://doi.org/10.3389/fspas.2022.858300

Diego, P., Piersanti, M., Laurenza, M., and Villante, U. (2020). Properties of solar wind structures at Mercury's orbit. *J. Geophys. Res.: Space Phys.*, *125*(9), e2020JA028281. https://doi.org/10.1029/2020ja028281

Duanmu, X. Y., Yao, Z. H., Wei, Y., and Ye, S. Y. (2023). Two types of mirror mode waves in the Kronian magnetosheath. *Earth Planet. Phys.*, *7*(3), 414–420. https://doi.org/10.26464/epp2023040

Eastman, T. E., Anderson, R. R., Frank, L. A., and Parks, G. K. (1981). Upstream particles observed in the Earth's foreshock region. *J. Geophys. Res.: Space Phys.*, *86*(A6), 4379–4395. https://doi.org/10.1029/JA086iA06p04379

Ge, Y. S., McFadden, J. P., Raeder, J., Angelopoulos, V., Larson, D., and Constantinescu, O. D. (2011). Case studies of mirror-mode structures observed by THEMIS in the near-Earth tail during substorms. *J. Geophys. Res.: Space Phys.*, *116*(A1), A01209. https://doi.org/10.1029/2010ja015546

Génot, V., Budnik, E., Hellinger, P., Passot, T., Belmont, G., Trávníček, P. M., Sulem, P. L., Lucek, E., and Dandouras, L. (2009). Mirror structures above and below the linear instability threshold: cluster observations, fluid model and hybrid simulations. *Ann. Geophys.*, *27*(2), 601–615. https://doi.org/10.5194/angeo-27-601-2009

Gershman, D. J., Dorelli, J. C., Vinas, A. F., Avanov, L. A., Gliese, U., Barrie, A. C., Coffey, V., Chandler, M., Dickson, C., … Burch, J. L. (2016). Electron dynamics in a subproton-gyroscale magnetic hole. *Geophys. Res. Lett.*, *43*(9), 4112–4118. https://doi.org/10.1002/2016gl068545

Goodrich, K. A., Ergun, R. E., Wilder, F. D., Burch, J., Torbert, R., Khotyaintsev, Y., Lindqvist, P. A., Russell, C., Strangeway, R., … Malaspina, D. M. (2016). MMS Multipoint electric field observations of small-scale magnetic holes. *Geophys. Res. Lett.*, *43*(12), 5953–5959. https://doi.org/10.1002/2016gl069157

Goodrich, K. A., Bonnell, J. W., Curry, S., Livi, R., Whittlesey, P., Mozer, F., Malaspina, D., Halekas, J., McManus, M., … Stevens, M. (2021). Evidence of subproton-scale magnetic holes in the Venusian magnetosheath. *Geophys. Res. Lett.*, *48*(5), e2020GL090329. https://doi.org/10.1029/2020gl090329

Greenstadt, E. W., Russell, C. T., and Hoppe, M. (1980). Magnetic field orientation and suprathermal ion streams in the Earth's foreshock. *J. Geophys. Res.: Space Phys.*, *85*(A7), 3473–3479. https://doi.org/10.1029/JA085iA07p03473

Hao, Y. F., Lu, Q. M., Gao, X. L., and Wang, S. (2016). Ion dynamics at a rippled quasi-parallel shock: 2D hybrid simulations. *Astrophys. J.*, *823*(1), 7. https://doi.org/10.3847/0004-637x/823/1/7

Hao, Y. F., Lu, Q. M., Gao, X. L., Wang, H. Y., Wu, D. J., and Wang, S. (2018). Two-dimensional hybrid simulations of filamentary structures and kinetic slow waves downstream of a quasi-parallel shock. *Astrophys. J.*, *861*(1), 57. https://doi.org/10.3847/1538-4357/aacb2c

Hao, Y. F., Lu, Q. M., Wu, D. J., and Xiang, L. (2023a). Wave activities throughout a low-Mach number quasi-parallel shock: 2-D hybrid simulations. *J. Geophys. Res.: Space Phys.*, *128*(5), e2023JA031295. https://doi.org/10.1029/2023ja031295

Hao, Y. F., Yang, Z. W., Tang, H. B., Kong, X. L., and Shan, L. C. (2023b). Particle-in-cell simulations of collisionless perpendicular shocks driven at a laser-plasma device. *AIP Adv.*, *13*(6), 065302. https://doi.org/10.1063/5.0142363

Hao, Y. F., Yang, Z. W., Guo, F., Liu, T. Z., Kong, X. L., Shan, L. C., and Wu, D. J. (2023c). Particle energization at a high Mach number perpendicular shock: 1D particle-in-cell simulations. *Astrophys. J.*, *954*(1), 18. https://doi.org/10.3847/1538-4357/ace69c

Hasegawa, A. (1969). Drift mirror instability in the magnetosphere. *Phys. Fluids*, *12*(12), 2642–2650. https://doi.org/10.1063/1.1692407

Haynes, C. T., Burgess, D., Camporeale, E., and Sundberg, T. (2015). Electron vortex magnetic holes: a nonlinear coherent plasma structure. *Phys. Plasmas*, *22*(1), 012309. https://doi.org/10.1063/1.4906356

Huang, S. Y., Sahraoui, F., Yuan, Z. G., He, J. S., Zhao, J. S., Le Contel, O., Deng, X. H., Zhou, M., Fu, H. S., and Shi, Q. Q. (2017). Magnetospheric multiscale observations of electron vortex magnetic hole in the turbulent magnetosheath plasma. *Astrophys. J. Lett.*, *836*(2), L27. https://doi.org/10.3847/2041-8213/aa5f50

Huang, S. Y., Sahraoui, F., Yuan, Z. G., Le Contel, O., Breuillard, H., He, J. S., Zhao, J. S., Fu, H. S., Zhou, M., and Deng, X. H. (2018). Observations of whistler waves correlated with electron-scale coherent structures in the magnetosheath turbulent plasma. *Astrophys. J.*, *861*(1), 29. https://doi.org/10.3847/1538-4357/aac831

Huang, S. Y., He, L. H., Yuan, Z. G., Sahraoui, F., Le Contel, O., Deng, X. H., Zhou, M., Fu, H. S., Jiang, K., … Burch, J. L. (2019). *MMS* observations of kinetic-size magnetic holes in the terrestrial magnetotail plasma sheet. *Astrophys. J.*, *875*(2), 113. https://doi.org/10.3847/1538-4357/ab0f2f

Jarvinen, R., Alho, M., Kallio, E., and Pulkkinen, T. I. (2020). Ultra-low-frequency waves in the ion foreshock of Mercury: a global hybrid modelling study. *Mon. Not Roy. Astron. Soc.*, *491*(3), 4147–4161. https://doi.org/10.1093/mnras/stz3257

Ji, X. F., Wang, X. G., Sun, W. J., Xiao, C. J., Shi, Q. Q., Liu, J., and Pu, Z. Y. (2014). EMHD theory and observations of electron solitary waves in magnetotail plasmas. *J. Geophys. Res.: Space Phys.*, *119*(6), 4281–4289. https://doi.org/10.1002/2014ja019924

Karlsson, T., Heyner, D., Volwerk, M., Morooka, M., Plaschke, F., Goetz, C., Hadid, L. (2021). Magnetic holes in the solar wind and magnetosheath near Mercury. *J. Geophys. Res.: Space Phys.*, *126*(5), e2020JA028961. https://doi.

org/10.1029/2020ja028961

Khrabrov, A. V., and Sonnerup, B. U. Ö. (1998). Error estimates for minimum variance analysis. *J. Geophys. Res.: Space Phys.*, *103*(A4), 6641–6651, https://doi.org/10.1029/97ja03731

Li, Z. Y., Sun, W. J., Wang, X. G., Shi, Q. Q., Xiao, C. J., Pu, Z. Y., Ji, X. F., Yao, S. T., and Fu, S. Y. (2016). An EMHD soliton model for small-scale magnetic holes in magnetospheric plasmas. *J. Geophys. Res.: Space Phys.*, *121*(5), 4180–4190. https://doi.org/10.1002/2016ja022424

Liu, H., Zong, Q. G., Zhang, H., Xiao, C. J., Shi, Q. Q., Yao, S. T., He, J. S., Zhou, X. Z., Pollock, C., … Rankin, R. (2019). MMS observations of electron scale magnetic cavity embedded in proton scale magnetic cavity. *Nat. Commun.*, *10*(1), 1040. https://doi.org/10.1038/s41467-019-08971-y

Madanian, H., Halekas, J. S., Mazelle, C. X., Omidi, N., Espley, J. R., Mitchell, D. L., and McFadden, J. P. (2020). Magnetic holes upstream of the Martian bow shock: MAVEN observations. *J. Geophys. Res.: Space Phys.*, *125*(1), e2019JA027198. https://doi.org/10.1029/2019JA027198

Maksimovic, M., Harvey, C. C., Santolik, O., Lacombe, C., de Conchy, Y., Hubert, D., Pantellini, F., Cornilleau-Werhlin, N., Dandouras, I., … Balogh, A. (2001). Polarisation and propagation of lion roars in the dusk side magnetosheath. *Ann. Geophys.*, *19*(10-12), 1429–1438. https://doi.org/10.5194/angeo-19-1429-2001

Meyer-Vernet, N. (2007). Bodies in the wind: dust, asteroids, planets and comets. In *Basics of the Solar Wind* (pp. 335–418). Cambridge: Cambridge University Press. https://doi.org/10.1017/CBO9780511535765.008

Philpott, L. C., Johnson, C. L., Anderson, B. J., and Winslow, R. M. (2020). The shape of Mercury's magnetopause: the picture from MESSENGER magnetometer observations and future prospects for BepiColombo. *J. Geophys. Res.: Space Phys.*, *125*(5), e2019JA027544. https://doi.org/10.1029/2019ja027544

Potapov, A. S. (2020). Kinetic magnetic holes in the high-speed streams during solar cycle 23. *Planet. Space Sci.*, *192*, 105066. https://doi.org/10.1016/j.pss.2020.105066

Romanelli, N., DiBraccio, G., Gershman, D., Le, G., Mazelle, C., Meziane, K., Boardsen, S., Slavin, J., Raines, J., … Espley, J. (2020). Upstream ultra-low frequency waves observed by MESSENGER's magnetometer: implications for particle acceleration at Mercury's bow shock. *Geophys. Res. Lett.*, *47*(9), e2020GL087350. https://doi.org/10.1029/2020gl087350

Russell, C. T., Jian, L. K., Luhmann, J. G., Zhang, T. L., Neubauer, F. M., Skoug, R. M., Blanco-Cano, X., Omidi, N., and Cowee, M. M. (2008). Mirror mode waves: messengers from the coronal heating region. *Geophys. Res. Lett.*, *35*(15), L15101. https://doi.org/10.1029/2008gl034096

Sentman, D. D., Thomsen, M. F., Gary, S. P., Feldman, W. C., and Hoppe, M. M. (1983). The oblique whistler instability in the Earth's foreshock. *J. Geophys. Res.: Space Phys.*, *88*(A3), 2048–2056. https://doi.org/10.1029/JA088iA03p02048

Shan, L. C., Mazelle, C., Meziane, K., Romanelli, N., Ge, Y. S., Du, A. M., Lu, Q. M., and Zhang, T. L. (2018). The quasi-monochromatic ULF wave boundary in the Venusian foreshock: Venus express observations. *J. Geophys. Res.: Space Phys.*, *123*(1), 374–384. https://doi.org/10.1002/2017ja024054

Shustov, P. I., Zhang, X. J., Pritchett, P. L., Artemyev, A. V., Angelopoulos, V., Yushkov, E. V., and Petrukovich, A. A. (2019). Statistical properties of sub-ion magnetic holes in the dipolarized magnetotail: formation, structure, and dynamics. *J. Geophys. Res.: Space Phys.*, *124*(1), 342–359. https://doi.org/10.1029/2018ja025852

Shustov, P. I., Nishimura, Y., Artemyev, A. V., Zhang, X. J., Angelopoulos, V., and Petrukovich, A. A. (2020). In-situ and optical observations of sub-ion magnetic holes. *J. Atmos. Solar-Terr. Phys.*, *208*, 105365. https://doi.org/10.1016/j.jastp.2020.105365

Solomon, S. C., McNutt, R. L. Jr., Gold, R. E., and Domingue, D. L. (2007). MESSENGER mission overview. *Space Sci. Rev.*, *131*(1-4), 3–39. https://doi.org/10.1007/s11214-007-9247-6

Sonnerup, B. U. Ö., and Cahill Jr, L. J. (1967). Magnetopause structure and attitude from Explorer 12 observations. *J. Geophys. Res.*, *72*(1), 171–183. https://doi.org/10.1029/JZ072i001p00171

Sonnerup, B. U. Ö., and Scheible, M. (1998). Minimum and maximum variance analysis. In G. Paschmann, et al. (Eds.), *Analysis Methods for Multi-Spacecraft Data* (pp. 185-220). Bern, Switzerland: International Space Science Institute.

Soucek, J., Lucek, E., and Dandouras, I. (2008). Properties of magnetosheath mirror modes observed by Cluster and their response to changes in plasma parameters. *J. Geophys. Res.: Space Phys.*, *113*(A4), A04203. https://doi.org/10.1029/2007ja012649

Stevens, M. L., and Kasper, J. C. (2007). A scale-free analysis of magnetic holes at 1 AU. *J. Geophys. Res.: Space Phys.*, *112*(A5), A05109. https://doi.org/10.1029/2006ja012116

Sun, J. C., Gao, X. L., Ke, Y. G., Lu, Q. M., Wang, X. Y., and Wang, S. (2019). Expansion of solar coronal hot electrons in an inhomogeneous magnetic field: 1D PIC simulation. *Astrophys. J.*, *887*(1), 96. https://doi.org/10.3847/1538-4357/ab5060

Sun, W. J., Shi, Q. Q., Fu, S. Y., Pu, Z. Y., Dunlop, M. W., Walsh, A. P., Zong, Q. G., Xiao, T., Tang, C. L., and Fazakerley, A. (2012). Cluster and TC-1 observation of magnetic holes in the plasma sheet. *Ann. Geophys.*, *30*(3), 583–595. https://doi.org/10.5194/angeo-30-583-2012

Sundberg, T., Burgess, D., and Haynes, C. T. (2015). Properties and origin of subproton-scale magnetic holes in the terrestrial plasma sheet. *J. Geophys. Res.: Space Phys.*, *120*(4), 2600–2615. https://doi.org/10.1002/2014ja020856

Tanaka, M., Goodrich, C. C., Winske, D., and Papadopoulos, K. (1983). A source of the backstreaming ion beams in the foreshock region. *J. Geophys. Res.: Space Phys.*, *88*(A4), 3046–3054. https://doi.org/10.1029/JA088iA04p03046

Tsurutani, B. T., Lakhina, G. S., Verkhoglyadova, O. P., Echer, E., Guarnieri, F. L., Narita, Y., and Constantinescu, D. O. (2011). Magnetosheath and heliosheath mirror mode structures, interplanetary magnetic decreases, and linear magnetic decreases: differences and distinguishing features. *J. Geophys. Res.: Space Phys.*, *116*(A2), A02103. https://doi.org/10.1029/2010ja015913

Turner, J. M., Burlaga, L. F., Ness, N. F., and Lemaire, J. F. (1977). Magnetic holes in the solar wind. *J. Geophys. Res.: Space Phys.*, *82*(13), 1921–1924. https://doi.org/10.1029/JA082i013p01921

Volwerk, M., Schmid, D., Tsurutani, B. T., Delva, M., Plaschke, F., Narita, Y., Zhang, T. L., and Glassmeier, K. H. (2016). Mirror mode waves in Venus's magnetosheath: solar minimum vs. solar maximum. *Ann. Geophys.*, *34*(11), 1099–1108. https://doi.org/10.5194/angeo-34-1099-2016

Volwerk, M., Goetz, C., Plaschke, F., Karlsson, T., Heyner, D., and Anderson, B. (2020). On the magnetic characteristics of magnetic holes in the solar wind between Mercury and Venus. *Ann. Geophys.*, *38*(1), 51–60. https://doi.org/10.5194/angeo-38-51-2020

Volwerk, M., Mautner, D., Wedlund, C. S., Goetz, C., Plaschke, F., Karlsson, T., Schmid, D., Rojas-Castillo, D., Roberts, O. W., and Varsani, A. (2021). Statistical study of linear magnetic hole structures near Earth. *Ann. Geophys.*, *39*(1), 239–253. https://doi.org/10.5194/angeo-39-239-2021

Wang, G. Q., Zhang, T. L., Volwerk, M., Schmid, D., Baumjohann, W., Nakamura, R., and Pan, Z. H. (2016). Mirror mode structures ahead of dipolarization front near the neutral sheet observed by Cluster. *Geophys. Res. Lett.*, *43*(17), 8853–8858. https://doi.org/10.1002/2016gl070382

Wang, G. Q., Zhang, T. L., Wu, M. Y., Schmid, D., Hao, Y. F., and Volwerk, M. (2020a). Roles of electrons and ions in formation of the current in mirror-mode structures in the terrestrial plasma sheet: magnetospheric multiscale observations. *Ann. Geophys.*, *38*(2), 309–318. https://doi.org/10.5194/angeo-38-309-2020

Wang, G. Q., Zhang, T. L., Wu, M. Y., Hao, Y. F., Xiao, S. D., Wang, G., Liu, L. J., Chen, Y. Q., and Volwerk, M. (2020b). Study of the electron velocity inside sub-ion-scale magnetic holes in the solar wind by MMS observations. *J. Geophys. Res.: Space Phys.*, *125*(10), e2020JA028386. https://doi.org/10.1029/2020ja028386

Wang, G. Q., Zhang, T. L., Xiao, S. D., Wu, M. Y., Wang, G., Liu, L. J., Chen, Y. Q., and Volwerk, M. (2020c). Statistical properties of sub-ion magnetic holes in the solar wind at 1 AU. *J. Geophys. Res.: Space Phys.*, *125*(10), e2020JA028320. https://doi.org/10.1029/2020ja028320

Wang, G. Q., Volwerk, M., Wu, M. Y., Hao, Y. F., Xiao, S. D., Wang, G., Liu, L. J., Chen, Y. Q., and Zhang, T. L. (2021a). First observations of an ion vortex in a magnetic hole in the solar wind by MMS. *Astron. J.*, *161*(3), 110. https://doi.

org/10.3847/1538-3881/abd632

Wang, G. Q., Volwerk, M., Xiao, S. D., Wu, M. Y., Chen, Y. Q., and Zhang, T. L. (2021b). Foreshock as a source region of electron-scale magnetic holes in the solar wind at 1 au. *Astrophys. J.*, *915*(1), 3. https://doi.org/10.3847/1538-4357/abfd31

Wang, G. Q., Volwerk, M., Du, A. M., Xiao, S. D., Wu, M. Y., Chen, Y. Q., and Zhang, T. L. (2021c). Statistical study of small-scale magnetic holes in the upstream regime of the Martian bow shock. *Astrophys. J.*, *921*(2), 153. https://doi.org/10.3847/1538-4357/ac1c07

Wang, G. Q., Volwerk, M., Xiao, S. D., Wu, M. Y., Hao, Y. F., Liu, L. J., et al. (2020d), Three-dimensional geometry of the electron-scale magnetic hole in the solar wind. *Astrophys. J. Lett., 904*(1), L11. https://doi.org/10.3847/2041-8213/abc553

Winslow, R. M., Anderson, B. J., Johnson, C. L., Slavin, J. A., Korth, H., Purucker, M. E., Baker, D. N., and Solomon, S. C. (2013). Mercury's magnetopause and bow shock from MESSENGER magnetometer observations. *J. Geophys. Res.: Space Phys.*, *118*(5), 2213–2227. https://doi.org/10.1002/jgra.50237

Wu, M. Y., Chen, Y. J., Du, A. M., Wang, G. Q., Xiao, S. D., Peng, E., Pan, Z. H., Chen, Y. Q., and Zhang, T. L. (2021). Statistical properties of small-scale linear magnetic holes in the Martian magnetosheath. *Astrophys. J.*, *916*(2), 104. https://doi.org/10.3847/1538-4357/ac090b

Yao, S. T., Shi, Q. Q., Li, Z. Y., Wang, X. G., Tian, A. M., Sun, W. J., Hamrin, M., Wang, M. M., Pitkänen, T., … Rème, H. (2016). Propagation of small size magnetic holes in the magnetospheric plasma sheet. *J. Geophys. Res.: Space Phys.*, *121*(6), 5510–5519. https://doi.org/10.1002/2016ja022741

Yao, S. T., Shi, Q. Q., Yao, Z. H., Li, J. X., Yue, C., Tao, X., Degeling, A. W., Zong, Q. G., Wang, X. G., … Giles, B. L. (2019a). Waves in kinetic-scale magnetic dips: MMS observations in the magnetosheath. *Geophys. Res. Lett.*, *46*(2), 523–533. https://doi.org/10.1029/2018gl080696

Yao, S. T., Shi, Q. Q., Yao, Z. H., Guo, R. L., Zong, Q. G., Wang, X. G., Degeling, A. W., Rae, I. J., Russell, C. T., and Tian, A. M. (2019b). Electron mirror-mode structure: magnetospheric multiscale observations. *Astrophys. J. Lett.*, *881*(2), L31. https://doi.org/10.3847/2041-8213/ab3398

Yao, S. T., Yue, Z. S., Shi, Q. Q., Degeling, A. W., Fu, H. S., Tian, A. M., Zhang, H., Vu, A., Guo, R. L., ... and Sun, W. J. (2021). Statistical properties of kinetic-scale magnetic holes in terrestrial space. *Earth Planet. Phys.*, *5*(1), 63–72. https://doi.org/10.26464/epp2021011

Zhang, T. L., Russell, C. T., Baumjohann, W., Jian, L. K., Balikhin, M. A., Cao, J. B., Wang, C., Blanco-Cano, X., Glassmeier, K. H., … Vörös, Z. (2008). Characteristic size and shape of the mirror mode structures in the solar wind at 0.72 AU. *Geophys. Res. Lett.*, *35*(10), L10106. https://doi.org/10.1029/2008gl033793